Prefabricated crack propagation in translucent alumina ceramic sheets during flame thermal shock

Qingxian Li, Yuqiao Li, Jia Li, Long Li, Xiaofeng Wu, Yingfeng Shao, Y. Charles, Salma Barboura, Fan Song

Prefabricated crack propagation in translucent alumina ceramic sheets during flame thermal shock

Qingxian Li[a,c,1], Yuqiao Li [a,c,1], Jia Li[b,*], Long Li[a,c], Xiaofeng Wu[d], Yingfeng Shao[a,c,*], Yann Charles[b], Salma Barboura[b], Fan Song[a,c]

[a]State Key Laboratory of Nonlinear Mechanics and Beijing Key Laboratory of Engineered Construction and Mechanobiology, Institute of Mechanics, Chinese Academy of Sciences, Beijing 100190, China

[b]Université Sorbonne Paris Nord, Laboratoire des Sciences des Procédés et des Matériaux, LSPM, CNRS, UPR 3407, F-93430, Villetaneuse, France

[c]School of Engineering Science, University of Chinese Academy of Sciences, Beijing 100049, China

[d]Beijing Institute of Structure and Environment Engineering, Beijing 100076, China

Abstract

The prefabricated cracks propagation of ceramic under flame thermal shock was studied by real-time observation. The experimental results show that wing cracks are generated from both tips of the prefabricated crack, and the complete failure of the samples is a high-speed process. The crack propagation speed is fast at first and then gradually slows down. The maximum propagation speed of the near flame tip increases with the prefabricated crack distance to the heated surface, while an inverse trend is observed for the far flame tip. The effect of prefabricated crack angle on thermal shock crack propagation was also considered. In addition, numerical simulations based on dynamic fracture mechanics were carried out to reproduce the entire cracking process. To this end, the relation between the dynamic stress intensity factors and the crack growth speed in the speed range of 100 m/s to 2600 m/s was identified by combing experiments and numerical simulations. The simulation results and the above-mentioned relation are consistent with the experimental observations. The numerical model can faithfully reproduce the crack evolution process of the thermal shock, which is difficult to observe in an experiment due to the high speed of the cracking process.

Keywords: Thermal shock; Crack speed; Dynamic stress intensity factor; Numerical simulation; Real-time

c	Specific heat capacity
C_r	Rayleigh wave speed
C_d	Elastic longitudinal wave speed
C_s	Elastic shear wave speed
E	Young's modulus
G	Quasi-static energy release rate of a crack

*Corresponding author. Tel.: +33 149402889; +86 10 82544360.
E-mail address: jia.li@univ-paris13.fr (J. Li); shaoyf@lnm.imech.ac.cn (Y.F. Shao)
1 These authors equally contributed to this work.

G_C^d	Critical dynamic energy release rate
G^d	Dynamic energy release rate
h	Air convection heat transfer coefficient
$k_p(V)$	Universal functions determined for p=I and II
K_C	Static critical energy release rate factor
K_C^d	Critical DSIF of the material
K_p	Quasi-static stress intensity factors of the fracture mode 'p'
K_p^d	Dynamic stress intensity factors of the fracture mode 'p'
Q	Heat flow
Δt	Time discretization step
T_0	Initial temperature of the plate
T_e	Environmental temperature
T_i	Temperature field
V	Speed of the crack tip
v	Poisson coefficient
ρ	Mass density
λ	Thermal conductivity
θ_c	Crack deviation angle with respect to the x-axis
σ_i	Stress field

1. Introduction

Ceramics have been widely used in the aerospace industry because of their good high-temperature strength, high hardness, high dielectric strength, and excellent tribology, etc. [1]. However, due to the brittleness of ceramics, thermal shock failure is easy to occur [2-5]. Therefore, thermal shock resistance has become one of the essential standards for selecting and designing ceramics.

Generally, to evaluate the thermal shock properties of materials, both cold shocks (water quenching [6-8]) or hot shocks (flame [9], laser [10], and irradiation [11]) are used. Crack morphology and residual strength of specimens are key parameters for assessing the thermal shock resistance of materials [6-11]. Take the classic example, Bahr et al. measured the crack morphology of the sample after water quenching [6], and Schneider et al. observed the crack morphology after irradiation [11].

With the in-depth study of the thermal-shock damage mechanism, it becomes crucial to determine the initiation and development of thermal shock damage. There is an urgent need for a method to observe the whole process of thermal shock cracking. Wang et al. dyed the ceramic cracks after thermal shock at different times to approximate the observation of crack propagation during thermal shock [3]. Based on avoiding the influence of the thermal shock process on crack capture, we used the

methods of water quenching and flame to observe the cold and hot shock cracking process of translucent materials in real time [12,13]. It is found that the speed of water quenching is slow, in the order of m/s. The speed of the flame thermal shock cracking process is fast, up to the order of km/s, i.e., dozens of times higher than that of Kobayashi's dynamic experiment [14]. Through cracks can be obtained under suitable conditions; this makes the hot shock a dangerous loading condition for ceramics materials.

Ceramic materials are prone to produce pores and microcracks in preparation and service, which will affect their thermal shock resistance. Previous thermal shock experimental studies related to prefabricated defects mainly focused on assessing cold shock performance with surface cracks. For example, Collin [15] and Meng [16] studied the propagation behavior of surface cracks in brittle materials after cold shock and then evaluated the thermal shock resistance of materials. There are few studies, however, on the influence of prefabricated defects on thermal shock performance under cold shock. For example, we reported for the first time the effect of prefabricated cracks of ceramics on thermal shock crack propagation under cold shock. We found that prefabricated cracks with different inclination angles affects both the probability of secondary cracks and the total vertical length of thermal shock cracks [17].

However, the real aerospace service environment of ceramics is very different from the experimental conditions of cold shock. Investigations on the effect of defects on crack growth under hot shock are still rare. So far, the relevant influence mechanism is not particularly clear. In addition, there are few simulations related to hot shock crack propagation, mainly focusing on cold shock crack propagation [18-24]. The possible reason is that the fracture mechanism is quite complex under hot shock, which involves the inertia effect and thermo-mechanical coupling process [24].

This work carried out experimental and numerical investigations on the crack propagation process of ceramic sheets containing a prefabricated crack under hot shock. To obtain the experimental results closer to the engineering practice, we used the designed flame thermal-shock real-time observation device to conduct the hot shock experiment on alumina samples with prefabricated cracks at different positions or with varying inclination angles. The entire hot shock-induced cracking process is recorded by using a high-speed camera. The effect of prefabricated cracks on the initiation and propagation of hot shock cracks under flame is observed and studied in real-time.

The propagation of thermal shock crack was simulated by establishing a model based on fracture mechanics. To reduce the computational effort, static stress intensity factors were evaluated at crack tips and then converted to dynamic stress intensity factors depending on crack moving speeds. We established an identification method by combining experiments and numerical simulations to determine the relationship between the critical dynamic stress intensity factor and crack moving speed. Then, based on this relationship, we simulate the entire hot shock-induced crack propagation process. The experiments show that the proposed model can faithfully reproduce the ceramic sheets' crack growth process during the hot shock.

2. Experimental procedure

2.1 Materials and preparation

We use 0.8 μm Al$_2$O$_3$ powder (99.4%, Jiawei Ceramics Co., Ltd., Zhuhai, China) to fabricate translucent alumina by tape casting and sintering in the hydrogen at 1700 ℃ for 2 h. The average grain size of ceramics is 20.8 μm, measured by the average line intercept method. The ceramic density measured by the drainage method is 3.95 g/cm^3. Ceramic sheets with a thickness of 0.5 mm, a width of 10 mm, and a length of 50 mm are used to ensure the formation of two-dimensional penetrated cracks. Prefabricated penetrated cracks are prepared on the sample's 10 mm×50 mm surface by a laser machine (JPT optoelectronics Co., Ltd., Shenzhen, China) with a power of 20 W and a scanning speed of 2 mm/s. The length of the prefabricated crack is 1mm, the width is 0.05 mm, and the inclination angles are 0, 26.6, 45, or 63.4°. The distance from the upper tip of the prefabricated crack to the heating interface is 3.5, 4, 4.5, and 6 mm. The morphology schematic of the sample is shown in Fig. 1.

2.2 Flame thermal shock test

To limit the flame on the heating surface only and not to affect the side observation of the initiation and propagation process of thermal shock crack, the oxyacetylene flame method is used to carry out a one-sided thermal shock on the sample. We clamp the ceramic sheet into a sandwich structure with two quartz glass fixtures and block the test flame with a graphite plate with a rectangular hole so that the ceramic sheet has only one 0.5 mm×50 mm face is heated by flame, as shown in Fig. 1.
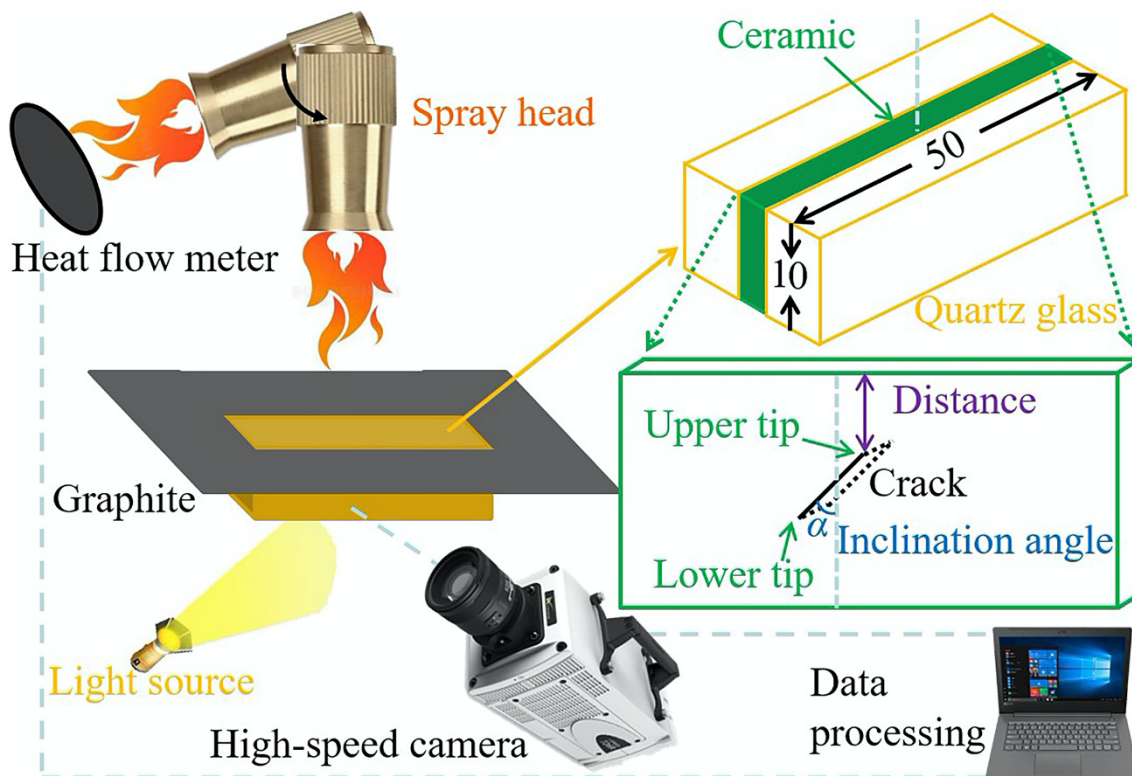

Fig. 1. Schematic diagram of processing sample and observation device for flame thermal shock.

The sample is placed on the worktable with a pre-focused position. The heat flux value of 2 MW/m² of flame is obtained by adjusting the flow of oxygen and acetylene and calibrating with a heat flow meter. Then the flame is aligned with the sample for the test. At this time, the high-speed camera (Phantom V2012, Wayne, NJ, USA) on the side of the sample captures the image during thermal shock at the speed of 651,000 frames/s, with a resolution of 128×64 pixels (the image is small and the definition is slightly poor at high speed), as shown in Fig. 1. By this method, using the light refraction and reflection at the crack interface, we successfully observed the initiation and propagation of wing cracks at the prefabricated cracks during thermal shock. From a series of images recorded in the experiment, we can obtain the crack propagation speed through the slope of the crack length curve in each frame. According to the characteristics of the crack image, we use different gray values to determine the crack tip. Because the resolution in the crack propagation direction is 128 pixels, the error of the crack tip is 10mm/128≈0.08mm, and the error of the corresponding speed is 50.7m/s.
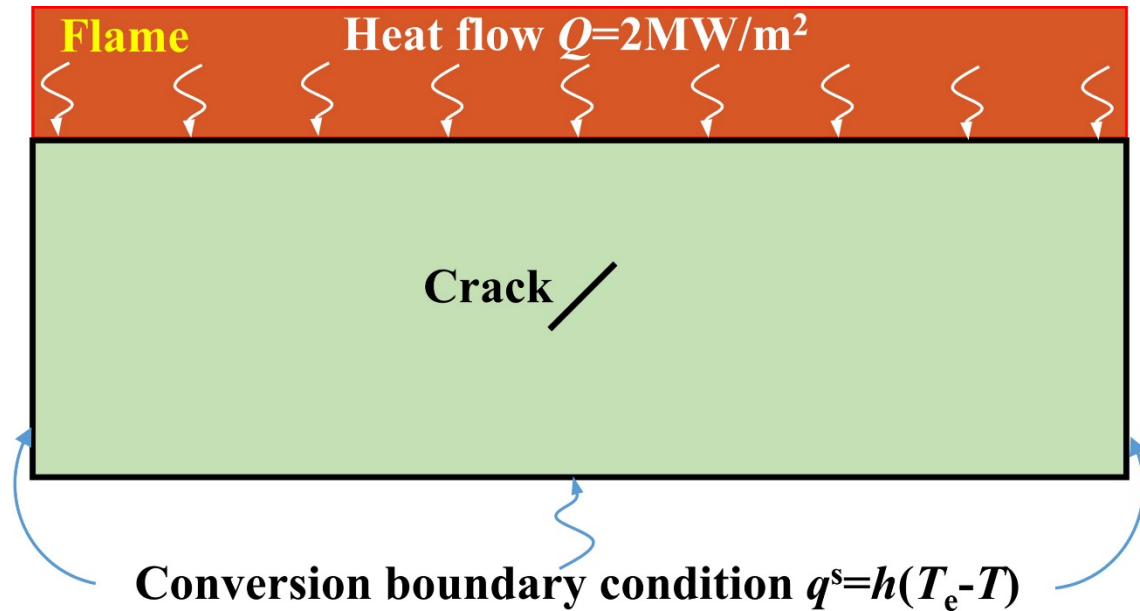

Fig. 2. Thermal boundary conditions.

3 Finite element modeling of thermal-shock cracking

3.1 Heat transfer problem

The temperature field of a ceramic plate under thermal shock is first evaluated using the finite element method as a heat transfer problem. The experimental conditions allow us to regard the temperature field as two-dimensional. The boundary conditions are illustrated in Fig. 2. The superior surface is subjected to a heat flow $Q \approx 2$ MW/m², while the other surfaces are considered as convective boundaries. We assume that the cracking process does not influence the temperature field. This assumption is justified because the cracking is a very fast process (within several microseconds) during which the temperature change in the plate is nearly negligible. The thermal parameters used in the simulations are the following ones [19,25,26]: mass density ρ=3950 kg/m³; thermal conductivity λ=31 W/(mK); specific heat capacity c=858 J/(kgK); air convection heat

transfer coefficient $h=20$ W/(m^2K); initial temperature of the plate $T_0=20°C$; environmental temperature $T_e=20°C$.

3.2 Dynamic Stress Intensity Factors (DSIF)

It was demonstrated that the dynamic stress intensity factors K_p^d of a moving crack in an infinite plate can be related to the quasi-static stress intensity factors K_p by [27]:

$$K_p^d = k_p(V)K_p \tag{1}$$

where V is the speed of the crack tip; $p=$I, II, III corresponding to the three fracture modes respectively. The functions $k_p(V)$, called universal functions, were determined for $p=$I and II, as [27]:

$$k_\mathrm{I}(V) \approx \frac{1-V/C_r}{\sqrt{1-V/C_d}} \qquad k_\mathrm{II}(V) \approx \frac{1-V/C_r}{\sqrt{1-V/C_s}} \tag{2}$$

Where C_r, C_d, and C_s are the Rayleigh wave speed, the elastic longitudinal wave speed, and the elastic shear wave speed, respectively. The dynamic energy release rate can be defined as in-plane stress:

$$G^d = \frac{\left(K_\mathrm{I}^d\right)^2+\left(K_\mathrm{II}^d\right)^2}{E} \tag{3}$$

where E is the Young's modulus of the material.

In practice, the quasi-static stress intensity factors K_I and K_II and the quasi-static energy release rate G of a crack can be determined by using the J-integral method combined with the finite element modeling. In this work, a variant of the J-integral, named A-integral, was used for its numerical conveniences [28]. This A-integral has the advantage of transforming a contour integral to a domain integral and therefore gains higher numerical accuracy.

3.3 Crack propagation criteria

In this work, we use the maximum circumferential stress criterion to predict the dynamic crack growth direction. For a semi-infinite moving crack along the x-axis, let (x, y) and (r, θ) be the Cartesian coordinates and the polar coordinates respectively with origin at the moving crack tip, the circumferential stress $\sigma_{\theta\theta}$ writes as follows [27]:

$$
\begin{aligned}
\sigma_{\theta\theta} &= \frac{K_\mathrm{I}^d B_\mathrm{I}}{\sqrt{2\pi}}\left\{[(S_1^2 - S_2^2) - (1 + S_1^2)\cos 2\theta]\frac{1}{\sqrt{r_1}}\cos\frac{\theta_1}{2} + \frac{4S_1 S_2}{1 + S_1^2}\cos 2\theta\frac{1}{\sqrt{r_2}}\cos\frac{\theta_2}{2}\right. \\
&\quad \left. - 2S_1\sin 2\theta\left(\frac{1}{\sqrt{r_1}}\sin\frac{\theta_1}{2} - \frac{1}{\sqrt{r_2}}\sin\frac{\theta_2}{2}\right)\right\} \\
&\quad + \frac{K_\mathrm{II}^d B_\mathrm{II}}{\sqrt{2\pi}}\left\{-2S_1\sin 2\theta\frac{1}{\sqrt{r_1}}\cos\frac{\theta_1}{2} + \frac{(1 + S_1^2)^2}{2S_2}\sin 2\theta\frac{1}{\sqrt{r_2}}\cos\frac{\theta_2}{2}\right. \\
&\quad - [(S_1^2 - S_2^2) - (1 + S_1^2)\cos 2\theta]\frac{1}{\sqrt{r_1}}\sin\frac{\theta_1}{2} \\
&\quad \left. - (1 + S_2^2)\cos 2\theta\frac{1}{\sqrt{r_2}}\sin\frac{\theta_2}{2}\right\}
\end{aligned}
$$

with:

$$S_1^2 = 1 - \frac{V^2}{C_d^2} \qquad\qquad S_2^2 = 1 - \frac{V^2}{C_s^2}$$

$$B_{\mathrm{I}} = \frac{1 + S_2^2}{4S_1 S_2 - (1 + S_2^2)^2} \qquad B_{\mathrm{II}} = \frac{2S_2}{4S_1 S_2 - (1 + S_2^2)^2}$$

and $r_1^2 = x^2 + S_1^2 y^2$, $r_2^2 = x^2 + S_2^2 y^2$, $r^2 = x^2 + y^2$, $\tan\theta_1 = S_1 \tan\theta$, $\tan\theta_2 = S_2 \tan\theta$.

According to the maximum circumferential stress criterion, the crack will deviate at an angle θ_c with respect to the *x*-axis, at which the maximum circumferential stress is maximal. This angle can be determined with the following conditions:

$$\frac{\partial\sigma_{\theta\theta}}{\partial\theta}(\theta_c) = 0 \text{ and } \sigma_{\theta\theta}(\theta_c) > 0 \tag{5}$$

the crack propagation criterion in the direction θ_c writes:

$$G^d(V) \le G_C^d(V); \;\; V \ge 0; \;\; V\left(G^d(V) - G_C^d(V)\right) = 0 \tag{6}$$

If we define an equivalent dynamic stress intensity factor:

$$K^* = \sqrt{\left(K_{\mathrm{I}}^d\right)^2 + \left(K_{\mathrm{II}}^d\right)^2} \tag{7}$$

And according to Eq. (3), the above criterion becomes:

$$K^*(V) \le K_C^d(V); \;\; V \ge 0; \;\; V\left(K^*(V) - K_C^d(V)\right) = 0 \tag{8}$$

In these expressions, G_C^d and K_C^d are the critical dynamic energy release rate and the critical DSIF of the material, modulated by the crack tip velocity *V*.

3.4 Global numeric algorithm

The cracking process under hot shock was simulated by establishing finite element models. The geometries of the tested samples were discretized by using 2D triangle elements. Fine meshes with an element size of about 0.02mm were used along the crack growth path to ensure simulation accuracy. The material parameters used in mechanical calculations, especially the static critical energy release rate factor, are estimated from the literature [14,25,29,30]. These parameters are: Young's modulus *E*=330GPa; Poisson coefficient *v*=0.22; static critical energy release rate factor K_C=3.5MPa$\sqrt{\mathrm{m}}$; longitudinal wave velocity C_d=9730m/s; shear wave velocity C_s=5829m/s; Rayleigh wave velocity C_r=5308m/s.

First, the time discretization step is set to Δt = 0.01 second before crack propagation. Temperature and stress fields are calculated by solving the heat transfer problem and the static thermo-elastic problem. Then, when the crack starts to propagate, a different algorithm is established to simplify the assessment of the dynamic crack propagation, which can be described as follows:

1. At each time step $t_{i+1} = t_i + \Delta t$, the time increment Δt is computed by $\Delta t = \Delta r / V_i$,

where Δr=0.05mm is a prescribed crack propagation distance used in the simulation; V_i is the fastest crack tip velocity of the previous time step;

2. Update the temperature field T_{i+1} (t_{i+1}) and the stress field $\sigma_{i+1}(t_{i+1})$ by resolving the heat transfer problem and the thermo-elasticity problem, respectively;

3. Calculate the quasi-static stress intensity factors of the crack tips and find the crack tip velocities V_{i+1} by solving the transcendent equation $K^*(V_{i+1}) = K_c^d(V_{i+1})$, where $K^*(V_{i+1})$ can be obtained from Eqs (1) and (7);

4. If $V_{i+1} \leq 0$, we set $V_{i+1} = 0$. There is no crack propagation;

5. Else, find the crack deviation angle θ_c according to Eqs (4) and (5) and determine the crack path. Create the new crack surfaces by updating the mesh near the moving crack paths before going to the next step.

3.5 Mesh adaptation

When the crack progresses, mesh near the moving crack tip should be modified to correctly represent the new crack lips. Numeral re-meshing technics have been used to model 2D or 3D crack growth [31,32]. In this work, a simplified re-meshing method was adopted to make the re-meshing task easier. The re-meshing process is roughly summarized as follows (Fig. 3):

1. Determine the crack growing path according to Eq. (4-5);

2. Find the intersections of the crack path with the element edges;

3. Move the nearest nodes to these intersections;

4. Double these nodes to create the new crack lips.
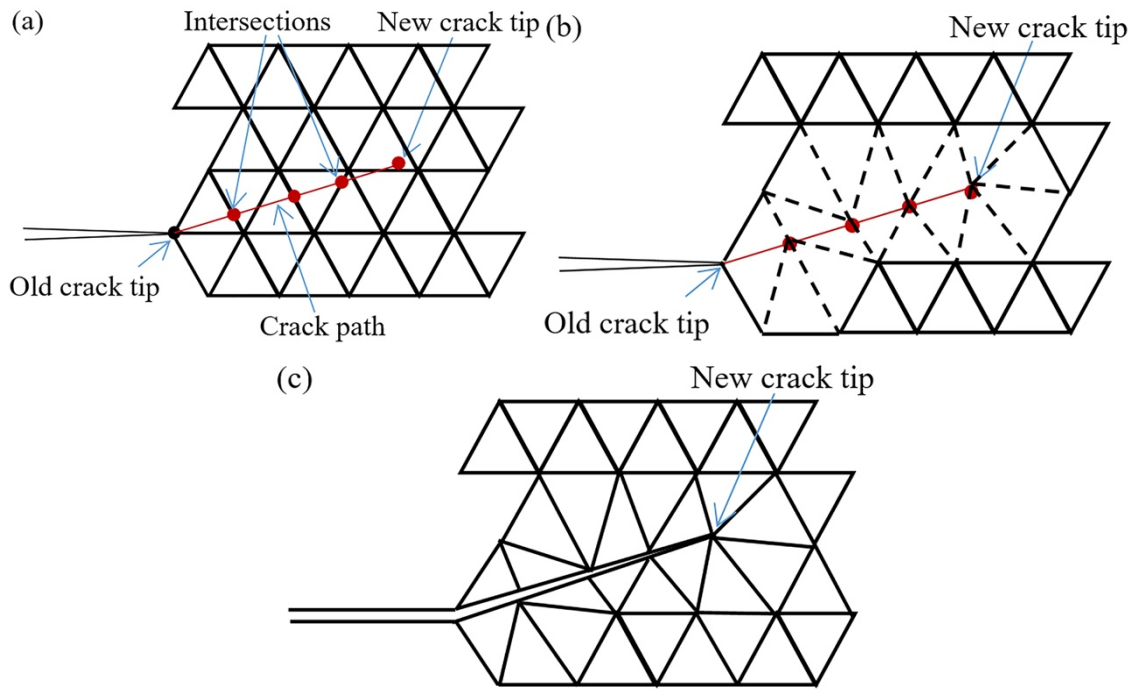
Fig. 3. Re-meshing procedure. (a) find the crack path and the intersection points, (b) move the nearest nodes to the intersection points, (c) doubling the intersection nodes to form the new mesh near the moving crack tip.

3.6 Estimation of $K_C^d(V)$

The crack growth velocity largely influences the dynamic crack toughness of a material. In the cases of the present work, no noticeable impact loading before crack growth is applied. Therefore, the critical DSIF at initial crack propagation $K_C^d(V=0)$ is set equal to the critical static SIF K_C. After the initial crack propagation, the dynamic crack toughness varies as a function of the crack velocity. For most materials, the critical DSIF increases as the crack velocity increases and thus forms a well-known Γ-shaped curve [33,34]. Experimental data relating crack velocity to the dynamic crack
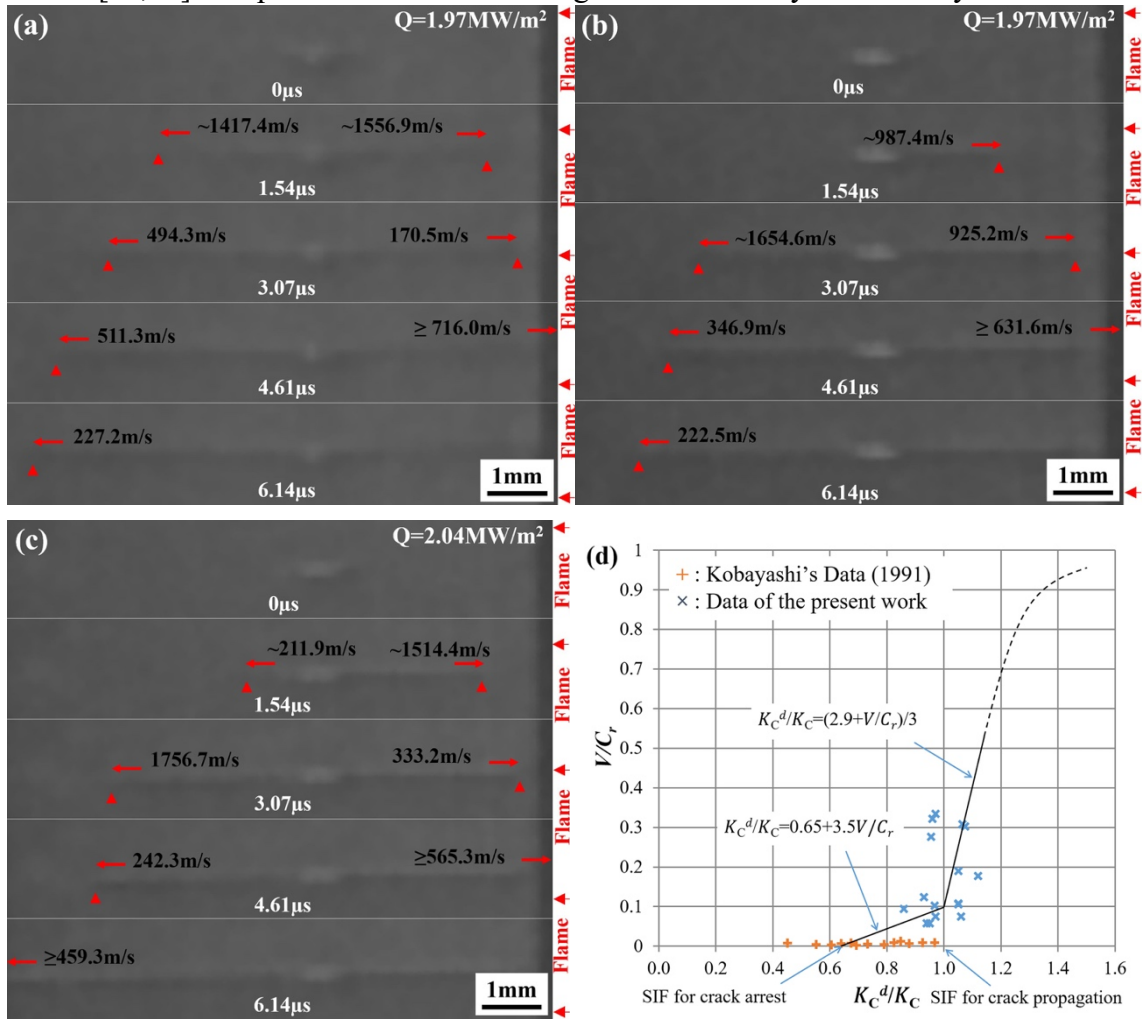
Fig. 4. Measured crack growth speeds of (a) specimen 1, (b) specimen 2, (c) specimen 3 for identification, with the speed error of 50.7m/s, and (d) Estimation of the $K_C^d - V$ relationship.
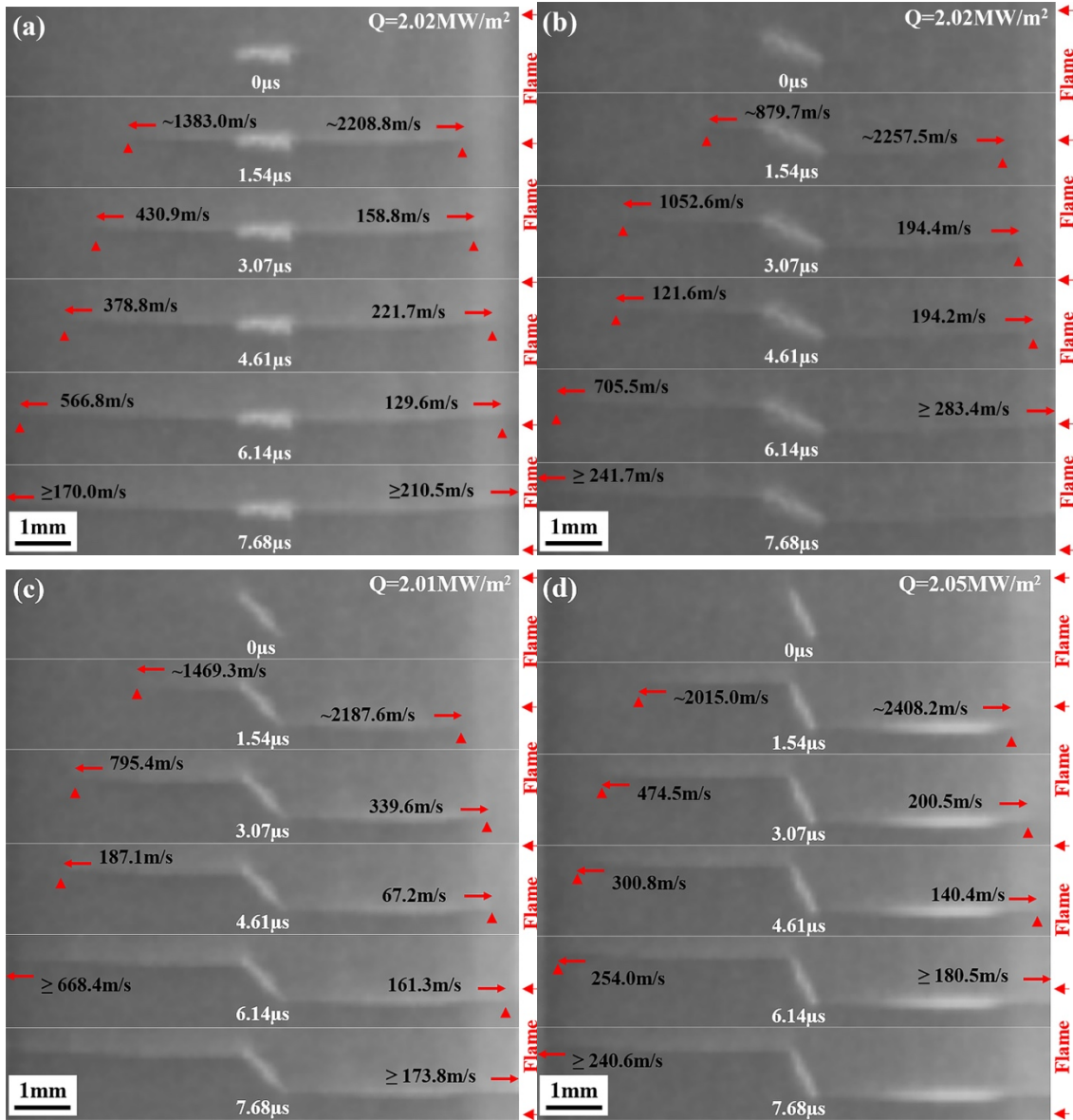
Fig. 5. Crack propagation process during flame thermal shock with the prefabricated crack angle of (a) 0, (b) 26.6, (c) 45 and (d) 63.4°, with the speed error of 50.7m/s, and a prefabricated crack distance of 4.5 mm.

toughness are still rare for ceramic materials. Experiments of Kobayashi on Al_2O_3 showed that the crack continues to propagate slowly at speeds ranging from 10 to 40 ms^{-1} [14], under a DSIF smaller than the static fracture toughness K_C. These results showed that the critical SIF for crack arrest K_C^a is smaller than K_C. However, as far as we know, experimental data for higher crack velocity are not available for Al_2O_3 in the literature. In the present work, these data are estimated from the thermal shock tests presented in Section 2.

Numerical simulations combined with the experimental results are used to identify the relationship between the dynamic crack toughness and the crack velocity. Among all the tested specimens, we have chosen three specimens for parameter identification, while the experimental results on other specimens are used to validate the numerical

model. The crack inclination angle of these specimens is 0°, and the distance between the upper crack tip and the heated surface is 4mm. The crack patterns at each camera shot and the measured cracking speeds of these specimens are presented in Fig.4a-c.

We use the following iterative procedure to estimate the $K_C^d - V$ relationship:

1. First, we apply the thermal loading on the finite element models with the initial cracks until $K=K_C$ at one crack tip;

2. Under this thermal loading and according to the crack tip positions recorded at different photographic times, we establish finite element models and calculate the corresponding static SIFs;

3. According to the recorded average crack tip velocities between two consecutive pictures, we calculate the DSIFs at crack tips, considered as the critical DSIFs. This result, combined with Kobayashi's experimental results normalized by the static SIF [14], allows us to estimate the first $K_C^d - V$ relationship, which is approached by a bilinear equation (Fig. 4d);

4. Based on this initial $K_C^d - V$ relationship, crack propagation simulations using the dynamic crack growth criterion Eq. (8) can be carried out. Numerical results on critical DSIFs $K_C^d(t)$ at crack tips are plotted as a function of time to calculate the averages between every two consecutive pictures;

5. The obtained average critical DSIFs with respect to the recorded average crack velocities are plotted to obtain a new $K_C^d - V$ relationship with which new complete crack propagation simulations are performed as described in step 4. Several iterations are necessary to reach a relative convergence of the $K_C^d - V$ relationship. The final obtained $K_C^d - V$ relationship is plotted in Fig. 4d.

It is worth noticing that the estimated $K_C^d - V$ relationship was established for crack speeds lower than $0.5C_r$, which may introduce unknown errors in predicting the cracking process if the crack speed is much higher.

4. Results and discussion

4.1 Effect of the prefabricated crack angle

We observed the flame thermal shock experiment of ceramic sheets with different prefabricated crack angles in real-time. Fig. 5 shows the thermal shock crack growth results with a prefabricated crack distance equal to 4.5 mm. We can see that the thermal shock crack initiation and propagation processes, with different prefabricated crack angles, are very similar. When the sample is subjected to flame thermal shock, wing cracks are generated from both tips of the prefabricated crack, and the cracks extend outward along the width direction of the sample. It is interesting to remark that whatever the initial inclination angle of the prefabricated crack, the wing crack propagation angle is about 0°. Usually, a through-width crack is formed in 4-5th frames, with the sample wholly damaged. For both crack tips, the overall growth process shows a "fast at first and then slow" growth trend, and the maximum growth speed seems to appear in the first frame. The maximum speed is about 30 times the one obtained in Kobayashi's dynamic experiment [14], highlighting our experiments' significance and

the proposed $K_C^d - V$ relationship.
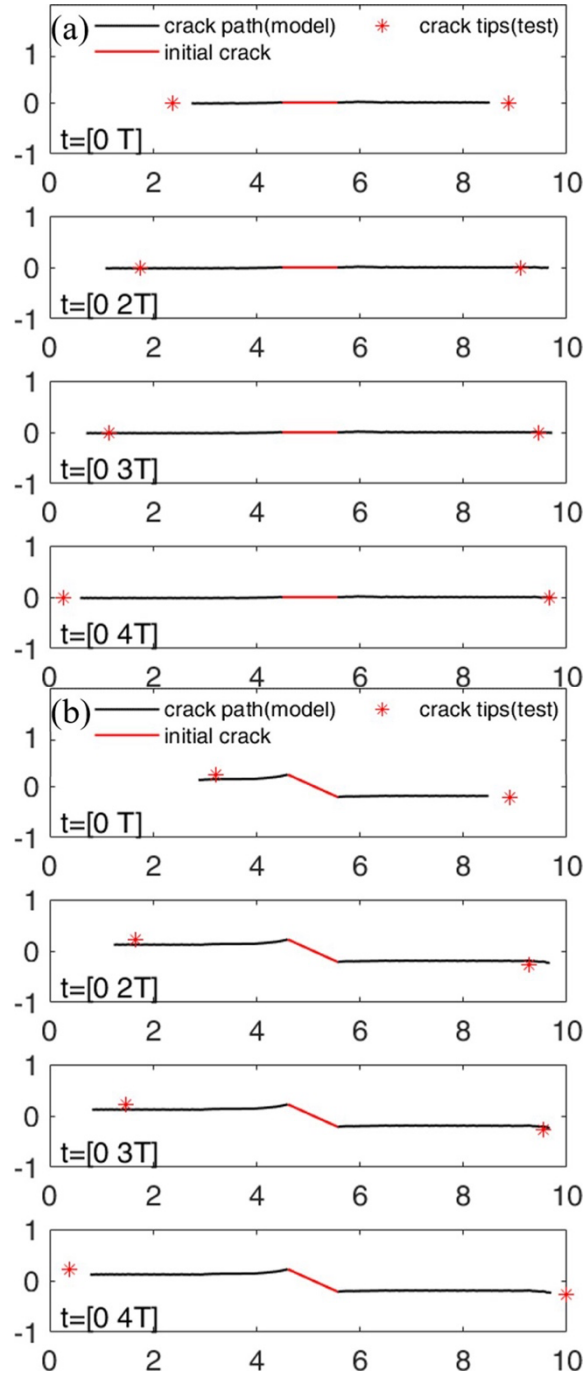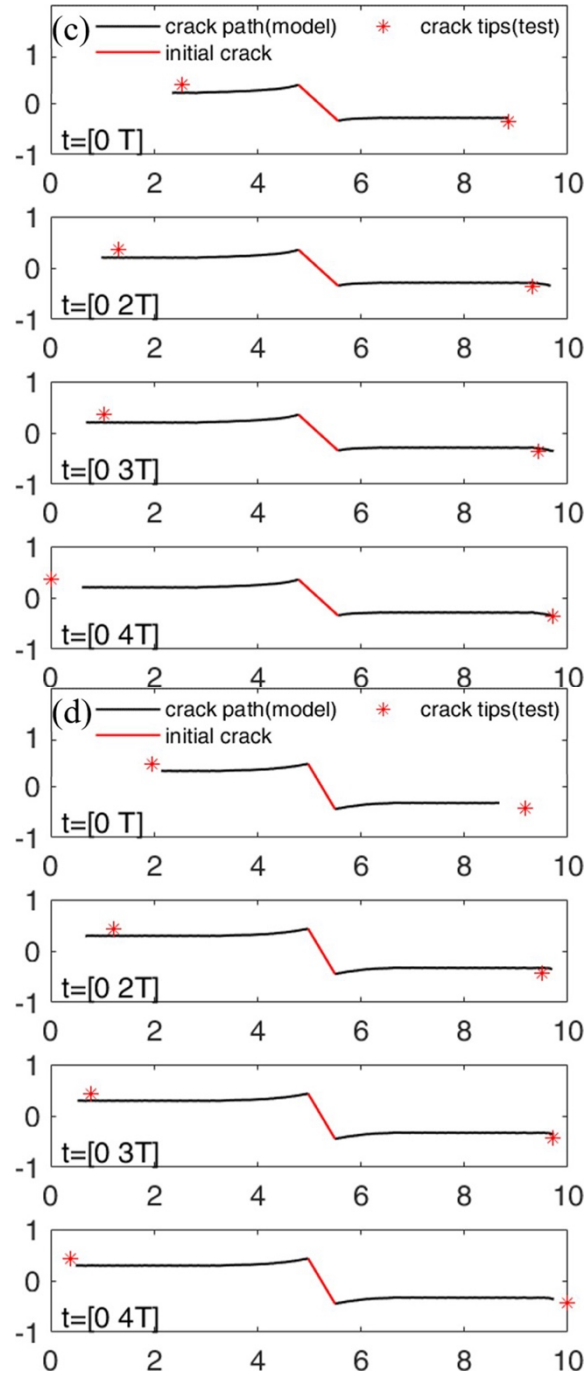
Fig. 6. Crack paths obtained from numerical simulations with the prefabricated crack angle of (a) 0, (b) 26.6, (c) 45 and (d) 63.4º, and a prefabricated crack distance of 4.5 mm.

The propagation speed is slightly different between cracks with different angles. The speed at both ends increases slightly with the increase of the inclination angle. Taking the upper crack tip as an example, the speed at the first frame increases from 2208 m/s at 0° to 2408 m/s at 63.4°, with an increase of 9.1%. In other words, the angle of prefabricated crack influences the hot shock-induced crack propagation at both tips, although not too significant. In addition, we can see that the upper crack tip's speed at the first frame is slightly faster than that of the lower crack tip.

It is interesting to remark the difference between the present work and the previous cold shock test results, using ceramic sheets with prefabricated cracks [17]. When the sample is subjected to cold shock, the cracks will initiate from the cold surface, expand inward, and interact with the prefabricated cracks. This difference is due to the stress field in the sample, which is different while using cold or hot shocks; the hot shock tends to produce cracks from the inside, while cold shock tends to initiate cracks from its surface.

The numerical simulations results on crack paths during the time $t=[0\ nT]$ are presented in Fig. 6, where n is the image's number and T is the period between two consecutive images ($T\approx1.54\ \mu s$). The crack tip positions measured from the recorded images are also plotted for comparison. From this figure, we can see that the numerical results are consistent with the experimental ones. That is, the sample starts to produce wing cracks from both tips of the prefabricated crack after being subjected to flame thermal shock, which then extends outward along the width of the sample.

The numerical model can reproduce the crack growth process with satisfactory accuracy for all the initial crack angles. It is worth noting that the experiments often provide instantaneously through cracks in samples, which the numerical simulations cannot predict. One reason may be that the evaluation of the DSIFs, according to Eq. (1), is established for a moving crack in an infinite plate. It is no longer accurate when the crack tip is close to the specimen edge.
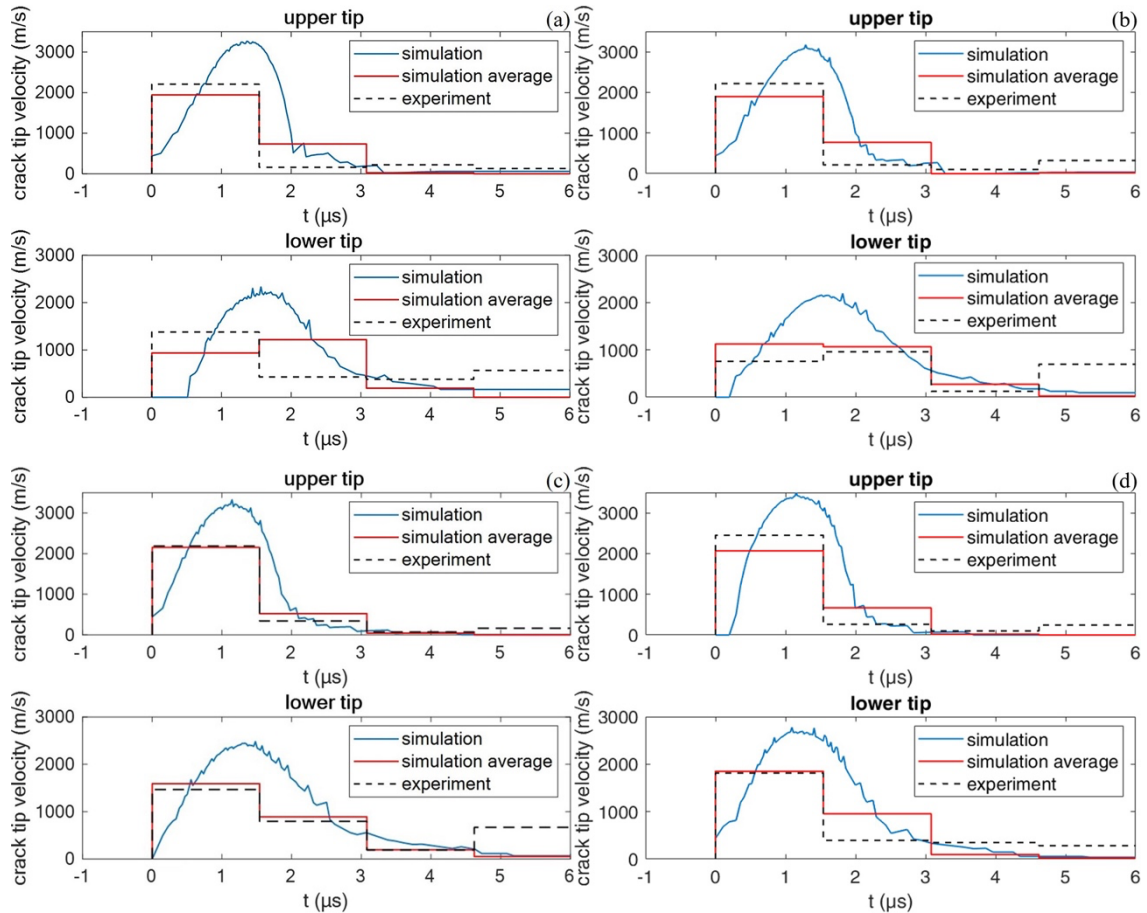
Fig. 7. Simulation of crack growth speed at both tips with the prefabricated crack distance of 4.5 mm and the prefabricated crack angle of (a) 0, (b) 26.6, (c) 45 and (d) 63.4^{o} during flame thermal shock.

As thermal shock cracking is a very fast process achieved within a few microseconds, the camera recording, using a finite number of images, can only provide an average cracking speed between two consecutive frames. On the contrary, numerical simulations allow for the evaluation of the crack propagation instantaneous speed. The crack propagation speed simulations at different crack angles, with a prefabricated crack distance of 4.5 mm, are shown in Fig. 7. Here again, we can see that the speed of the simulated thermal-shock crack propagation process is very close to the experimental results. That is, the cracking speed quickly increases from zero to a maximal value, then decreases as the crack tip approaches the sample edge. We can see that the propagation speed of the upper tip at the first frame is slightly faster than that at the lower tip. This result is also in good agreement with the experimental recording. In addition, the simulation results show that the increase of prefabricated crack angle leads to an increase in the initial propagation speed of both crack tips. We can also get this trend from experiments, but further investigations are needed to confirm experimental dispersion.

4.2 Effect of the prefabricated crack distance

Fig. 8 shows the thermal-shock crack growth morphology variation with the distance of the prefabricated crack (set as 3 mm, 4 mm, and 6 mm, respectively). In combination with Fig. 5a, the maximum average growth speed between two consecutive frames of the upper tip gradually increases with the distance from the heating interface, e.g., from about 750 m/s for a distance equal to 3 mm, up to about 2600 m/s for 6 mm. However, the propagation speed of the lower tip seems to decrease with the increase of the distance from the heated surface. In addition, some tests show that the wing crack first appears at the top tip of the crack, as shown in Fig. 8b and c.
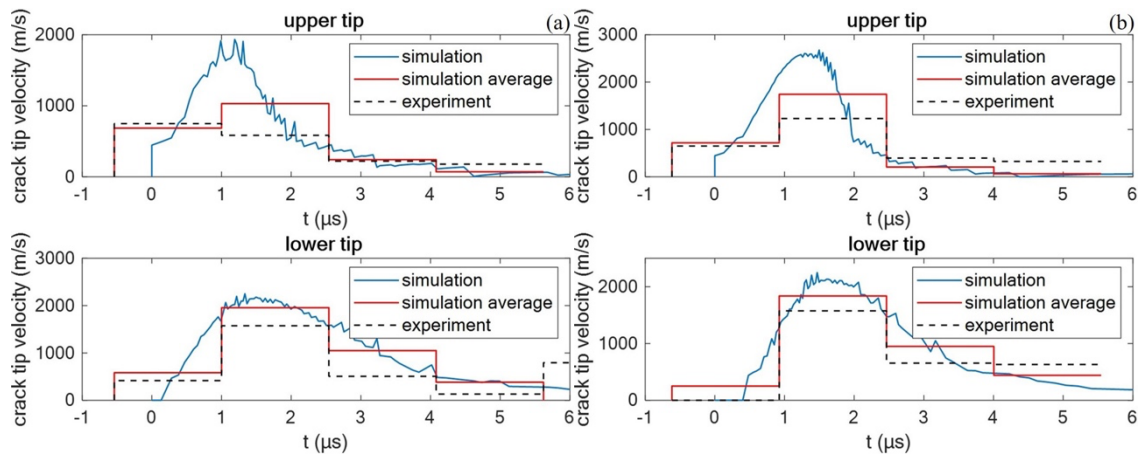
Fig.9 shows the thermal shock crack growth speed with the different prefabricated crack distances in the samples during the flame thermal shock by numerical simulation.
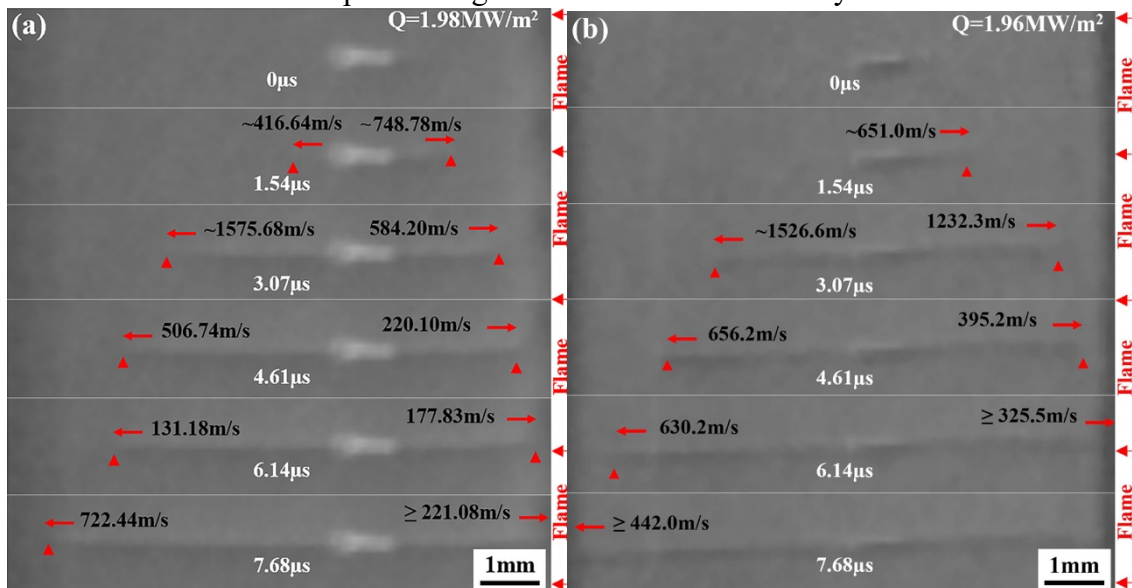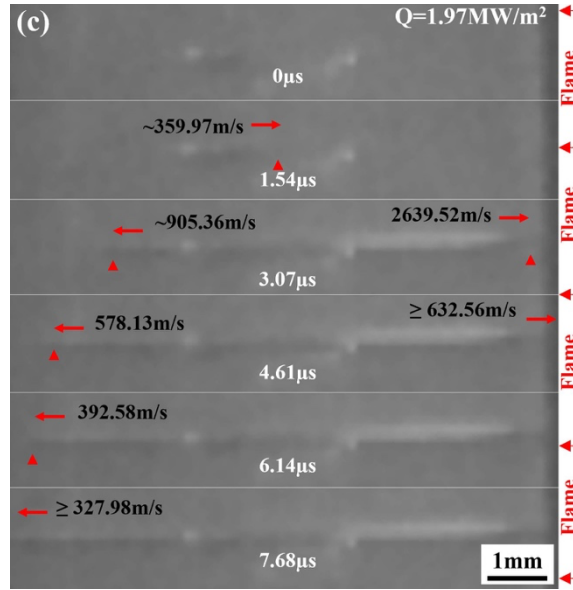
Fig. 8. Thermal shock crack propagation process during flame thermal shock when the upper tip distance of prefabricated crack is (a) 3, (b) 4, and (c) 6 mm, with the speed error of 50.7m/s.

Combined with Fig. 7a, we can observe that the maximum growth speed of the upper crack tip increases with the distance from the heated surface. On the contrary, the maximum propagation speed of the lower crack tip decreases with this distance. These results are in concordance with the experiments presented above. Besides, comparing the speed curves of the upper and the lower tips, we can see that the upper tip tends to initiate wing crack earlier than the lower tip, which is also consistent with the experimental results.
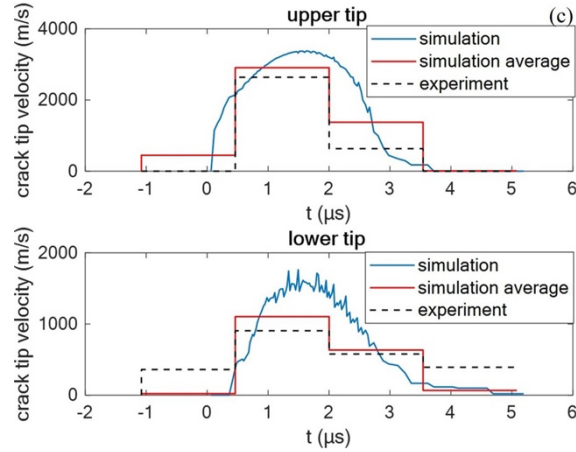
Fig. 9. Simulation of thermal shock crack growth speed at both tips with the prefabricated crack distance of (a) 3, (b) 4, and (c) 6 mm during flame thermal shock.

5. Conclusions

We carried out flame thermal shock experiments on ceramic sheets with prefabricated cracks and observed them in real-time. The results show that the wing cracks start from both tips of the prefabricated crack and propagate to both sides under flame thermal shock. The maximum propagation speed occurs in the first two frames, and then the speed decreases rapidly. The maximum crack growth speed of the upper tip increases with the distance of the prefabricated crack, while the lower tip decreases. Besides, the maximum propagation speed of both tips increases slightly with the prefabricated crack angle.

Finite element models were built to simulate the crack growth of high speed under hot shock based on fracture mechanics. To this end, we first obtained an estimation of the $K_C^d - V$ relationship of alumina ceramics at higher speeds, combining experiments and numerical simulations. The simulation results based on dynamic fracture mechanics can faithfully reproduce the evolution process of thermal shock cracking and are consistent with the experimental observations. It is found that the relation of speed first increases and then decreases with time during the initiation and propagation of thermal shock cracks, which is difficult to obtain experimentally due to the limitation of the shooting speed of a high-speed camera. It is also confirmed that the upper tip tends to occur wing crack earlier than the lower tip in the different prefabricated crack distance calculations. This current theoretical numerical experimental study in ceramics allows us a deeper understanding of the formation and evolution of thermal shock crack modes.

Acknowledgments

References

[1] Padture NP, Gell M, Jordan EH. Materials science-Thermal barrier coatings for gas-turbine engine applications. Science 2002;296:280-284. https://doi.org/10.1126/science.1068609.

[2] Han JC, Wang BL. Thermal shock resistance of ceramics with temperature-dependent material properties at elevated temperature. Acta Mate 2011;59:1373-1382. https://doi.org/10.1016/j.actamat.2010.10.068.

[3] Wang AZ, Hu P, Du B, Fang C, Zhang DY, Zhang XH. Cracking behavior of ZrB_2-SiC-Graphite sharp leading edges during thermal shock. Ceram Int 2018;44:7694-7699. https://doi.org/10.1016/j.ceramint.2018.01.195.

[4] Pompe WE. Thermal shock behavior of ceramic materials-modeling and measurement. in: Schneider GA, Petzow G, editors. Thermal shock and thermal fatigue behavior of advanced ceramics, 1993.

[5] Wang YW, Xia B, Su HH, Chen H, Feng X. Improving the thermal shock resistance of ceramics by crack arrest blocks. Sci China Technol Sc 2016;59:913-919. https://doi.org/10.1007/s11431-015-5978-x.

[6] Bahr HA, Fischer G, Weiss HJ. Thermal-shock crack patterns explained by single and multiple crack-propagation. J Mater Sci 1986;21:2716-2720. https://doi.org/10.1007/BF00551478.

[7] Yoshimoto T, Ishihara S, Goshima T, McEvily AJ, Ishizaki T. An improved method for the determination of the maximum thermal stress induced during a quench test. Scripta Mater 1999; 41:553-559. https://doi.org/10.1016/S1359-6462(99)00185-2.

[8] Li DY, Li WG, Zhang WB, Fang DN. Thermal shock resistance of ultra-high temperature ceramics including the effects of thermal environment and external constraints. Mater Design 2012;37:211-214. https://doi.org/10.1016/j.matdes.2011.12.047.

[9] Levine SR, Opila EJ, Halbig MC, Kiser JD, Singh M, Salem JA. Evaluation of ultra-high temperature ceramics for aeropropulsion use. J Eur Ceram Soc 2002;22:2757-2767. https://doi.org/10.1016/S0955-2219(02)00140-1.

[10] Jian CY, Hashida T, Takahashi H, Saito M. Thermal shock and fatigue resistance evaluation of functionally graded coating for gas turbine blades by laser heating method. Compos Eng 1995;5:879-889. https://doi.org/10.1016/0961-9526(95)00041-K.

[11] Schneider GA, Petzow G. Thermal shock testing of ceramics-a new testing method. J Am Ceram Soc 1991;74:98-102. https://doi.org/10.1111/j.1151-2916.1991.tb07303.x.

[12] Li YQ, Li QX, Wu XF, Shao YF, Li L, Song F. Cracking in the translucent alumina ceramic during flame thermal shock. Ceram Int 2021;47:30974-30979. https://doi.org/10.1016/j.ceramint.2021.07.154.

[13] Shao YF, Song F, Liu BY, Li W, Li L, Jiang CP. Observation of ceramic cracking during quenching. J Am Ceram Soc 2017;100:520-523. https://doi.org/10.1111/jace.14674.

[14] Kobayashi AS. Dynamic fracture of ceramics and ceramic composites. Mater Sci Eng A 1991;143:111-117. https://doi.org/10.1016/0921-5093(91)90730-B.

[15] Collin M, Rowcliffe D. Analysis and prediction of thermal shock in brittle materials. Acta Mater 2000;48:1655-1665. https://doi.org/10.1016/S1359-6454(00)00011-2.

[16] Meng SH, Jin H, An J, Bai GH, Xie WH. Mechanism analysis of thermal shock properties for ZrB_2-20%SiC_p-10%AlN ultra-high temperature ceramic with the surface defects. Solid State Sci 2010;12:1667-1671. https://doi.org/10.1016/j.solidstatesciences.2010.07.020.

[17] Li YQ, Liu BY, Wang XH, Shao YF, Li L, Wei JC, Song F. The effect of a prefabricated crack on the crack growth in ceramics during quenching. Ceram Int 2021;47:3643-3648. https://doi.org/10.1016/j.ceramint.2020.09.215.

[18] Ricardo LFF, Leguillon D, Parry G, Doitrand A. Modeling the thermal shock induced cracking in ceramics. J EUR CERAM SOC 2020;40:1513-1521. https://doi.org/10.1016/j.jeurceramsoc.2019.11.071.

[19] Li J, Song F, Jiang CP. Direct numerical simulations on crack formation in ceramic materials under thermal shock by using a non-local fracture model. J Eur Ceram Soc 2013;33:2677-2687. https://doi.org/10.1016/j.jeurceramsoc.2013.04.012.

[20] Chu DY, Li X, Liu ZL. Study the dynamic crack path in brittle material under thermal shock loading by phase field modeling. Int J Fract 2017;208:115-130. https://doi.org/10.1007/s10704-017-0220-4.

[21] Wang YT, Zhou XP, Kou MM. An improved coupled thermo-mechanic bond-based peridynamic model for cracking behaviors in brittle solids subjected to thermal shocks. Eur J Mech A-Solid 2019;73:282-305. https://doi.org/10.1016/j.euromechsol.2018.09.007.

[22] Bourdin B, Marigo JJ, Maurini C, Sicsic P. Morphogenesis and propagation of complex cracks induced by thermal shocks. Phys Rev Lett 2014;112. https://doi.org/10.1103/PhysRevLett.112.014301.

[23] Tang SB, Zhang H, Tang CA, Liu HY. Numerical model for the cracking behavior of heterogeneous brittle solids subjected to thermal shock. Int J Solid Struct 2016;80:520-531. https://doi.org/10.1016/j.ijsolstr.2015.10.012.

[24] Wang YT, Zhou XP, Kou MM. Numerical studies on thermal shock crack branching instability in brittle solids. Eng Fract Mech 2018;204:157-184. https://doi.org/10.1016/j.engfracmech.2018.08.028.

[25] Jiang CP, Wu XF, Li J, Song F, Shao YF, Xu XH, Yan P. A study of the mechanism of formation and numerical simulations of crack patterns in ceramics subjected to thermal shock. Acta Mater 2012;60:4540-4550. https://doi.org/10.1016/j.actamat.2012.05.020.

[26] Liang JZ, Qiu YL. Thermal conductivity of graphite-filled LDPE composites. Polym Bull 2015;72:1723-1734. https://doi.org/10.1007/s00289-015-1366-8.

[27] Freund LB. Dynamic fracture mechanics. New York: Cambridge University Press; 1998.

[28] Petit C, Vergne A, Zhang X. A comparative numerical review of cracked materials. Eng Fracture Mech 1996;54:423-439. https://doi.org/10.1016/0013-7944(95)00145-X.

[29] Krell A, Pippel E, Woltersdorf J, Burger W. Subcritical crack growth in Al2O3 with submicron grain size. J Eur Ceram Soc 2003;23:72-79. https://doi.org/10.1016/S0955-2219(02)00072-9.

[30] Belenky A, Bar-On I, Rittel D. Static and dynamic fracture of transparent nanograined alumina. J Mech Phys Solids 2010;58:484-501. https://doi.org/10.1016/j.jmps.2010.02.002.

[31] Tradegard A, Nilsson F, Ostlund S. FEM-remeshing technique applied to crack growth problems. Comput Methods Appl Mech Engrg 1998;160:115-131. https://doi.org/10.1016/S0045-7825(97)00287-9.

[32] Branco R, Antunes FV, Costa JD. A review on 3D-FE adaptive remeshing techniques for crack growth modeling. Eng Fract Mech 2015;141:170-195. https://doi.org/10.1016/j.engfracmech.2015.05.023.

[33] Kobayashi AS, Ramulu M. Dymaic fracture mechanics. J Aero Soc Of India 1985;37:1-19.

[34] Kobayashi AS, Ramulu M, Dadkhah MS, Yang KH, Kang BSJ. Dynamic fracture toughness. Int J Fract 1986;30:275-285. https://doi.org/10.1007/BF00019707.

Figure Captions:

Fig. 1. Schematic diagram of processing sample and observation device for flame thermal shock.

Fig. 2. Thermal boundary conditions.

Fig. 3. Re-meshing procedure. (a) find the crack path and the intersection points, (b) move the nearest nodes to the intersection points, (c) doubling the intersection nodes to form the new mesh near the moving crack tip.

Fig. 4. Measured crack growth speeds of (a) specimen 1, (b) specimen 2, (c) specimen 3 for identification, with the speed error of 50.7m/s, and (d) Estimation of the $K_C^d - V$ relationship.

Fig. 5. Crack propagation process during flame thermal shock with the prefabricated crack angle of (a) 0, (b) 26.6, (c) 45 and (d) 63.4°, with the speed error of 50.7m/s, and a prefabricated crack distance of 4.5 mm.

Fig. 6. Crack paths obtained from numerical simulations with the prefabricated crack angle of (a) 0, (b) 26.6, (c) 45 and (d) 63.4°, and a prefabricated crack distance of 4.5 mm.

Fig. 7. Simulation of crack growth speed at both tips with the prefabricated crack distance of 4.5 mm and the prefabricated crack angle of (a) 0, (b) 26.6, (c) 45 and (d) 63.4° during flame thermal shock.

Fig. 8. Thermal shock crack propagation process during flame thermal shock when the upper tip distance of prefabricated crack is (a) 3, (b) 4, and (c) 6 mm, with the speed error of 50.7m/s.

Fig. 9. Simulation of thermal shock crack growth speed at both tips with the prefabricated crack distance of (a) 3, (b) 4, and (c) 6 mm during flame thermal shock.